Optical Super-Localisation of Single Nanoparticle Nucleation and Growth in Nanodroplets

Paolo Ciocci+,[a] Dimitrios Valavanis+,[b] Gabriel N. Meloni,[b, c] Jean-François Lemineur,[a] Patrick R. Unwin,*[b] and Frédéric Kanoufi*[a]

The formation of metal nanoparticles (NPs) on surfaces by electrodeposition is of significant interest, particularly with a view to understand the early stages of nucleation and growth. Here, the combination of scanning electrochemical cell microscopy (SECCM) and interference reflection microscopy (IRM) is demonstrated to be a compelling approach for real-time monitoring of NP dynamics within the SECCM meniscus-electrode wetted area, through synchronous monitoring in the millisecond range of the electrochemical and optical signatures. Diffraction-limited entities, undergoing phase changes at the electrode substrate, are readily highlighted and tracked in time, including the onset time for the appearance of NPs and their movement over time. The results strongly implicate the rapid formation, surface diffusion and aggregation of smaller entities (not detectable optically) to produce the larger electrodeposited NPs. By applying SECCM tips of different size, it is also possible to understand how the wetted area (meniscus size) plays a key role in the number of NPs formed, with small tip sizes allowing the formation of single NPs. The SECCM-IRM approach is expected to be a powerful platform for the study of myriad phase-formation processes at the nanoscale, particularly by drawing on the possibility of making hundreds or thousands of measurements in fresh surface locations through SECCM technology.

Introduction

The functionalization of surfaces with nanoparticles (NPs) is of considerable interest for myriad applications across science, and understanding the underlying mechanisms is essential for the rational design and fabrication of functional interfaces.[1,2] The assembly of NPs at defined regions of a surface can be achieved via top-down (vapour deposition) and bottom-up (assembly of pre-synthesised NPs) approaches.[3–5] The physical confinement of growing NPs and the capture of fully formed NPs using a physical trap or template has also been explored.[6] Precise local delivery of NPs can be achieved by several techniques, notably by dip-pen nanolithography, which uses the tip of a scanning probe microscope to guide and deliver NPs.[7]

Pipette-based techniques, with a tuneable pipette opening size ranging from micrometres to nanometres in diameter, have been used to manipulate, count and size individual NPs confined within the pipette opening.[8–10] They have also been used to deliver (coat) NPs onto a solid surface immersed in electrolyte baths.[11,12] Alternatively, the electrolyte meniscus, formed at the pipette orifice and in contact with an electrode surface, can act as a well-defined miniature electrochemical cell as in the scanning electrochemical cell microscopy (SECCM) technique, used for a range of electrodeposition or electro-crystallisation processes, and also for the controlled delivery of various types of nanocolloids onto specific locations on electrodes.[13–22] As well as investigating NP nucleation/growth processes,[22,23] SECCM[15] offers an elegant way to manufacture (electrochemically-driven) nanostructures, with optimal electrical connection between the structures and the substrate surface.[24] For example, using high reactant concentrations and high electrodeposition rates, it becomes possible to print 3D micro- to nanostructures with sub-100 nm resolution.[16,18,19]

At lower electrodeposition rates, SECCM could enable the printing of arrays of NPs on electrode surfaces, by electro-depositing them one by one. Indeed, SECCM was recently proposed as tool for fabricating on-demand arrays of individual Ag NPs.[20] In-situ optical microscopy, which is becoming increasingly powerful in electrochemistry,[25,26] would be a natural complement for such studies, by enabling operando monitoring of the electrodeposition process to reveal mechanistic aspects in real time. Herein, interference reflection microscopy (IRM), is used to synchronously observe events, occurring inside the SECCM droplet cell, during the electrodeposition of Ag NPs onto an indium tin oxide (ITO) electrode. This approach

[a] P. Ciocci,+ Dr. J.-F. Lemineur, Dr. F. Kanoufi
Université Paris Cité
ITODYS, CNRS
F-75013 Paris (France)
E-mail: frederic.kanoufi@u-paris.fr
[b] D. Valavanis,+ Dr. G. N. Meloni, Dr. P. R. Unwin
Department of Chemistry
University of Warwick
Coventry CV4 7AL (United Kingdom)
E-mail: p.r.unwin@warwick.ac.uk
Homepage: https://warwick.ac.uk/fac/sci/chemistry/research/
electrochemistry/
[c] Dr. G. N. Meloni
Institute of Chemistry
Department of Fundamental Chemistry
University of São Paulo
05508-000 São Paulo, SP (Brazil)
[+] These authors contributed equally to this work.

ChemElectroChem

Research Article
doi.org/10.1002/celc.202201162

**Chemistry
Europe**
European Chemical
Societies Publishing

reveals NP dynamics, which are mechanistically informative, and allows us to determine how droplet size controls the NP number distribution. More generally, this work advances the coupling of in-situ optical techniques to pipette electrochemistry.[25–31]

Results and Discussion

The hybrid SECCM-IRM methodology[27] is depicted in Figure 1a. Experimental details and pictures of the experimental setup are provided in the Experimental Section and in the Supporting Information, SI, section S1. In short, a pipette with an opening of ca. 600 nm diameter (D) was filled with an electrolyte solution containing 5 mM $AgNO_3$ in 0.1 M KNO_3 and a Ag/AgCl quasi-reference counter electrode (QRCE) was loaded from the back. The pipette (SECCM tip) was approached to the ITO-coated glass substrate, which was connected as the working electrode (WE). A 0.2 V bias was applied between the WE and the QRCE, so that no Ag^+ reduction (Ag electrodeposition) would occur upon meniscus contact of the pipette with the WE.

Meniscus contact was detected by a charging spike in the current trace (see Figures S2.1 and S2.2 in section S2, SI) that immediately halted the pipette approach. After a short 0.3 s quiet period, at the approach potential, the WE potential was then stepped to −0.8 V for 0.7 s. At this potential, the nucleation probability on ITO[20] is close to 1, so the process is limited by the surface density of nucleation sites. The switch to the reducing potential is marked as time 0 s. The electrodeposition of Ag at the WE surface, whose area is defined by the SECCM meniscus contact, resulted in a current transient, as portrayed in Figure S3.1 (section S3, SI). At the end of the deposition period, the WE potential was stepped back to 0.2 V while the pipette was retracted from the surface. The procedure, lasting overall ca. 4.5 s per deposition, was repeated at fresh sites a desired number of times. Further details about the full sequence are provided in the SI, section S2.

To limit the deposition to a single, or few NPs, per landing site, the SECCM wetted area should be selected according to the density of nucleation sites. For Ag NP electrodeposition on the ITO surface, although dependent on the electrodeposition overpotential, the NP density σ_{NP} is reported in the 10^8 to $5\times$
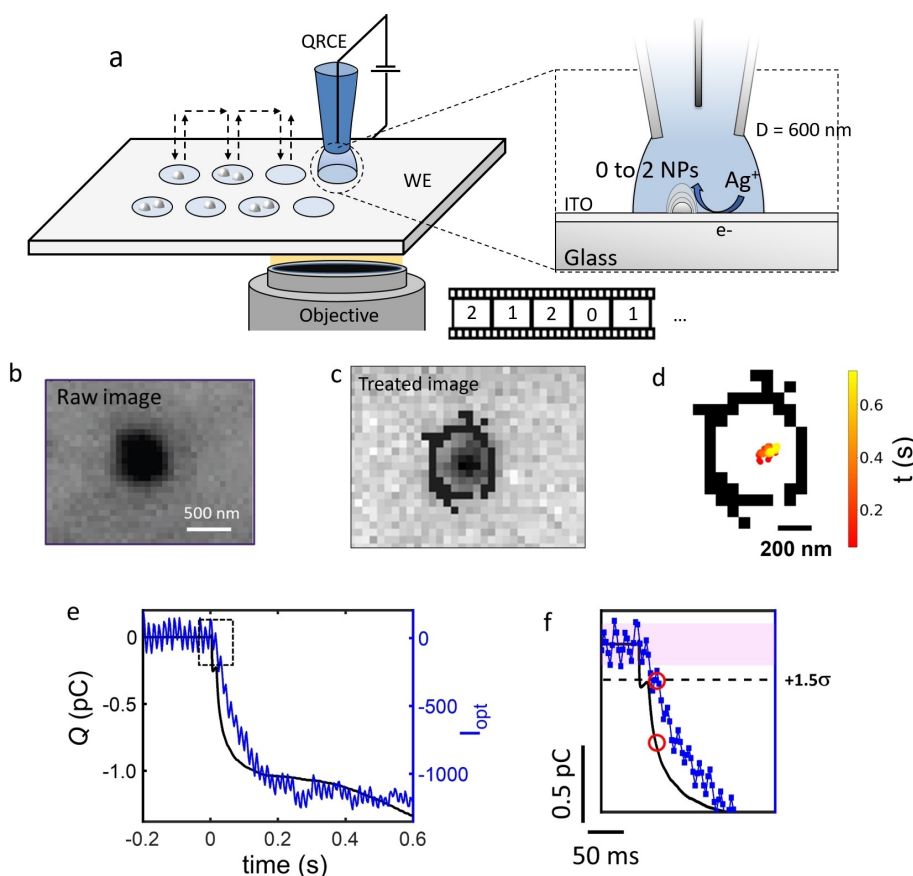
Figure 1. (a) Schematic of the hybrid SECCM-IRM experimental setup used for electrodepositing Ag NPs, within individual nanodroplet electrochemical cells, while synchronously monitoring optically (IRM) the process. (b) Image of the ITO-coated glass coverslip upper interface, showing the footprint (dark region) of the SECCM wetted area. (c) A diffraction limited dark-contrasted optical feature is revealed within the wetted area perimeter (noted in black). The feature's centroid is super-localised and its intensity is integrated over a 4×4 pixel region around the centroid. (d) Displacement (coloured trace) of the optical feature centroid, within the wetted area perimeter (noted in black), during the electrodeposition process. (e) Electrochemical charge Q (integrated area under the current-time curve) and optical intensity I_{opt} traces comparison, enabling limit of detection to be estimated. (f) Zoomed-in area of (e). The shaded pink area corresponds to one standard deviation (1 σ) of the optical signal and the optical limit of detection is set at 1.5 σ (vertical dotted line). The detection in the I_{opt} trace and the corresponding point in the Q trace are marked with red circles.

ChemElectroChem

Research Article
doi.org/10.1002/celc.202201162

**Chemistry
Europe**
European Chemical
Societies Publishing

10^9 NPs per cm^2 range.[32,33] Hence, a single NP would nucleate over a 0.02 to 1 μm^2 electrode area (equivalent disc diameter of 160 to 1100 nm), well within the range of probe fabrication, as the SECCM wetted area approximates the dimensions of the pipette opening.[27] Importantly, this length scale is also compatible with the imaging resolution of optical microscopes. With a 63× magnification oil immersion objective (numerical aperture, NA = 1.4) and a λ = 470 nm wavelength illumination, as used here, it is theoretically possible to resolve objects separated by $\lambda/(2NA)$ = 168 nm. Optical microscopy can then image the presence of an individual NP within an individual nanodroplet. This is accomplished with IRM by acquiring images of the upper interface of the glass coated ITO substrate, while operating the inverted microscope in reflection mode. Temporal resolution was achieved by recording images at a rate of 327.5 frames per seconds (3 ms resolution) synchronously with the electrochemical current obtained at a 68 μs temporal resolution (see details in SI section S1). Figure 1b shows a typical IRM image of the SECCM meniscus, recorded at the end of the electrodeposition procedure. The meniscus is detected optically in the raw image as a region of intensity darker than the surrounding background (see also the optical trace over the full sequence in Figure S2.1). This is related to the difference in refractive index (n) between the electrolyte ($n \approx 1.33$) and the air ($n = 1$), making, from Fresnel formalism of the reflection at optical interfaces, the wetted region of ITO less reflective than the ITO/air interface.

Image processing algorithms[27,28,30,34] were used to visualize, operando, the Ag electrodeposition process over time, with sub-droplet resolution (algorithms description in section S4). A movie was obtained for this experiment (Movie S1) from which the image in Figure 1c was extracted and reveals the presence of a dark contrasted feature, optically resolved within a ca. 0.39 μm^2 area droplet. This suggests that the electrodeposition produced a single Ag NP, in excellent agreement with an independent report at comparable experimental conditions, and particularly with the reported post mortem AFM/SEM images.[20]

Herein, IRM provides the opportunity for operando monitoring of several descriptors of the growing NP over time. On each image of the time series, the optical feature is super-localized: its centroid coordinates are obtained, with ∼10 nm precision (see details in SI section S4). Thus, the lateral motion of the centroid can be tracked dynamically. In this event, there is < 100 nm movement in the centroid position across the deposition period (Figure 1d). While centroid motion can be a proxy for NP motion, for diffraction-limited NPs, it can also be indicative of asymmetric NP growth mechanisms.[35–39] We consider such descriptor analysis in more detail below, for the case of multiple interacting NPs.

Integration over a 4×4 pixel region of interest (ROI) centred at the NP centroid (Figure 1c) provides the feature's optical intensity trace, I_{opt} (Figure 1e) overlaid with the evolution of the electrochemical charge trace, Q, calculated from Figure S3.1 by integration. Before the potential step, I_{opt} is within the noise level, but the step in potential to −0.8 V results in the appearance of the dark contrasted feature that progressively

darkens (decrease in I_{opt}). The optical intensity is usually a descriptor of the locally deposited mass (or a power law of the mass, depending on the type of optical microscopy[26]). Evidently, I_{opt} tracks the evolution of Q. From the final accumulated charge Q_f = 1.45 pC, the equivalent final diameter (d_{NP}) of the NP can be estimated:

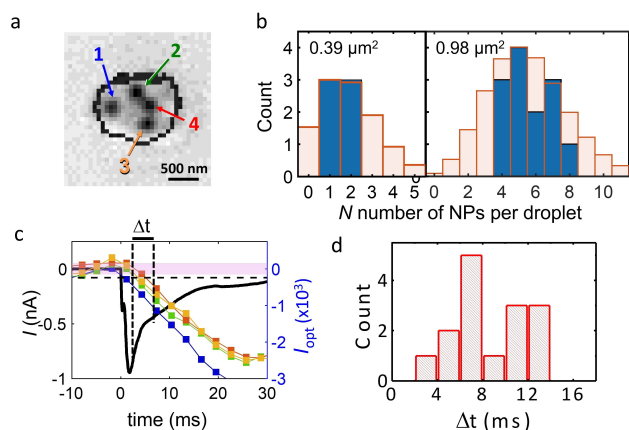$$d_{NP} = 2\left(\frac{3Q_f V_{m,Ag}}{2\pi FN}\right)^{\frac{1}{3}} \tag{1}$$

assuming N hemispherical NPs are deposited and using $V_{m,Ag}$ = 10.27 cm^3 mol^{-1} the molar volume of Ag, and F the Faraday constant. From Equation (1), for N = 1 NP detected, the NP produced in Figure 1 is equivalent to an hemispherical NP of final diameter of 83 nm.

We can estimate an optical limit of detection from the accumulated charge at the point where the optical intensity is different from the background value. In Figure 1f, the shaded pink area corresponds to one standard deviation (1 σ) of the I_{opt} trace and the optical limit of detection is set at 1.5 σ. In the synchronised Q trace, it corresponds to an accumulated charge of ∼0.6 pC or, from Equation (1), an equivalent hemispherical NP of diameter of 63 nm.

The experiment was performed at 9 different approach locations (full sequence in section S2), and 6 successful landings, i.e., unambiguous SECCM meniscus contact with the ITO substrate, were analysed. The SECCM meniscus formation was rather reproducible throughout, with an average footprint area, estimated from the IRM images, of 0.39 ± 0.06 μm^2. The average Q_f was 2 ± 0.6 pC. However, it is important to point out that within these nanometric droplets, it was possible to resolve between N = 1 or 2 NPs, which is a key strength of the SECCM-IRM technique (see below): an example of droplet with 2 NPs is given in Figure S3.3.

To explore the effect of electrodeposition area on the number of NPs formed, we made an experimental array of electrodeposition at 12 landing sites using a ca. 1 μm diameter SECCM tip, resulting in a ca. 0.95 μm^2 wetted area (2.4 times the area of the previous experiment). An example of an image-processed optical movie for this experiment is provided in the SI as Movie S2; while Figure 2a is a processed optical image recorded at the end of the electrodeposition step for one of the landing sites (additional electrochemical and optical data in section S5, SI). Four different NPs are clearly resolved in this image and marked in the figure. The distribution of the number of NPs optically resolved at each landing site is provided in Figure 2b giving an average σ_{NP} of 5 ± 1 NPs per μm^2. The average NP equivalent diameter, estimated from the final charge for each electrodeposition spot and using Equation (1), with N derived from the number of optical features, is 95 ± 10 nm.

Scanning electron microscopy (SEM) images, recorded post mortem, of electrodeposition events using an even larger SECCM tip, resulting in a droplet of ca. 4 μm^2, were compared with corresponding IRM images (see Figure S6). The larger droplet ensured correct identification of the NPs constellation to permit analysis of the accuracy of the multi-microscopy

ChemElectroChem

Research Article
doi.org/10.1002/celc.202201162

Chemistry Europe
European Chemical
Societies Publishing

Figure 2. (a) Processed optical image of a larger droplet cell (diameter of 1.1 μm, area 0.95 μm²) showing 4 NPs at the end of the Ag electrodeposition. (b) Calculated Poisson probability to find N NPs in a droplet of area 0.39 or 0.98 μm² (light red bars, left and right panel, respectively) together with the number of NPs experimentally counted (blue bars). (c) Comparison of the total electrochemical current and the optical intensity traces for the four NPs that grow inside the droplet cell. The shaded pink area and the dotted lines correspond to 1 and 1.5 times the standard deviation of the optical signal, respectively, the latter being used to evaluate the detection delay Δt. (d) Distribution of detection delays between first and last NPs detected in different droplet cells.

cross-correlation.[28] Both IRM and SEM images give a $\sigma_{NP} \sim 6$ NPs per μm² in good agreement with the values observed in smaller droplets. This average NP density value was further used to calculate a theoretical Poisson distribution $P(N)$ representing the probability of finding N = 0, 1, 2… Ag NPs into a droplet of surface area A_d, as shown in Equation (2):[40]

$$P(N) = \frac{(A_d \sigma_{NP})^N e^{-A_d \sigma_{NP}}}{N!} \qquad (2)$$

The Poisson distribution is superimposed in Figure 2b (shaded bars) on the experimental histograms obtained for the 0.39 and 0.98 μm² wetted area droplets. For both cases, the number of NPs detected per droplet experimentally matches reasonably to the calculated distribution.

The growth of multiple NPs per droplet in the 0.98 μm² area case provides further insights into the electrodeposition process. The optical intensity traces of each NP in Figure 2c (full scale in Figure S5.1) follow a similar pattern of I_{opt} decreasing with time, tracking the electrochemical charge reported in Figures S5.2. It suggests that the four NPs have similar growth dynamics (obviously not possible to determine from the electrochemical signal in the case of multiple NPs) and grow to a similar final size.

The synchronous optical monitoring of NP growth can further elucidate early-stage NP evolution (Figure 2c). The onset of optical detection for each NP can be estimated by extrapolation (by linear fitting) of the individual optical traces, using the same criterion as used to evaluate the limit of optical detection in Figure 1f. The four NPs in Figure 2c are detected ($I_{opt} > 1.5\,\sigma$ from the background) sequentially within an extrapolated time interval, $\Delta t \approx 5$ ms in the order, NP #1 (blue

trace), NP #2 (green trace) NP #3 (orange trace) and NP #4 (red trace) in a third frame (see consecutive images in Figure S5.3). The distribution of the extrapolated time interval between first and last NP onset, Δt evaluated for all experiments, is given in Figure 2d, and ranges from 3 to 13 ms.

The electrochemical current-time signal is characteristic of charging of the SECCM cell and diffusion-limited mass transport to the electrode surface on the timescale accessed, suggesting rapid formation of multiple Ag nuclei across the electrode surface.[15] This is followed by NP growth (from the optical signal) implying an aggregation mechanism.[22,23,41] In this scenario, the optical onset time relates to the formation of measurable NPs by aggregation of smaller, undetectable clusters or smaller NPs:[15] the onset time in the 3–15 ms range is then characteristic of the dynamics of cluster surface diffusion to make the observed NPs. Noteworthy, while transmission electron microscopy (TEM) would offer higher spatial resolution imaging, metallic nanoclusters requires atomic-level and high temporal resolution imaging. The growth and motion of Au nanoclusters was indeed demonstrated by ex situ imaging of the same region of an electrode sequentially polarized, rinsed, TEM-imaged, at 5, 10 and 30 ms.[41] In situ TEM imaging, with 5 nm Ag NP visualization (not sufficient to image nanoclusters), was reported.[42] However, unlike the SECCM-optical microscopy configuration proposed here, it may lack of generalization: it is limited to strongly confined liquid-cell (50 nm thickness of liquid), with > 2 orders of magnitude lower temporal resolution (1 frame per second) and required high electron radiation (energy and dose) used to induce rachiochemically the reduction of Ag^+ and growth of NPs.[42]

Further support for this mechanism is obtained from analysis of the centroid position over time for individual NPs. As depicted in Figure 3a among the 4 NPs (from Figure 2), the topmost and the leftmost NPs move radially outwards, while the other 2 are apparently drifting around the same position. The range of NP displacement, Δd_c, across all experiments and SECCM tip sizes, is depicted by the distribution in Figure 3b, using initial and final positions to extract Δd_c, since no complex movements were detected. The maximum Δd_c observed was ca. 210 nm, with the majority of values being smaller than the respective NP dimensions.

Proposed cases of nuclei surface diffusion and NP asymmetric growth by aggregation are drawn in Figure 3c. Outwards radial growth for NPs close to the meniscus perimeter, as observed in Figure 3a, is reasoned to result from a local slower mass transport rate (local confinement) at the SECCM meniscus edge,[27] with further NP growth at these locations driven by aggregation, rather than electrodeposition.

The direction of the asymmetric growth of the NP (centroid displacement) is evaluated from a growth angle. An angle of 0° indicates a centroid displacement towards the centre of the wetted area, while an angle of 180°, a displacement towards the edge. The polar histogram of the centroid displacement angle is given in Figure 3d for all experiments and for displacements $\Delta d_c > 30$ nm. It shows some preference for movement towards the edge, with NPs #1 and #2 in Figure 3a being examples of such movement.
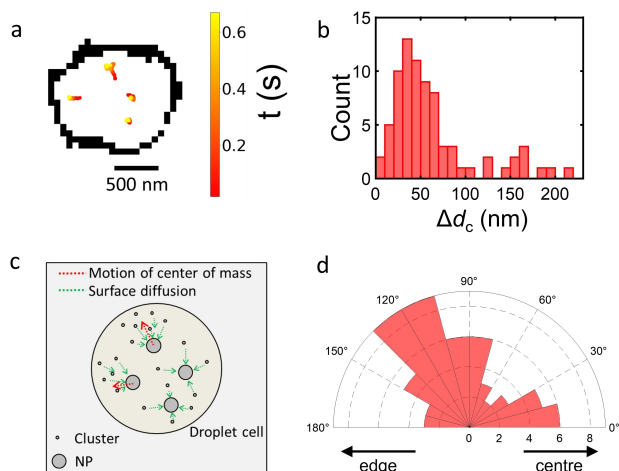
Figure 3. (a) Displacement (coloured traces) of the centroids of the optical features, within the wetted area perimeter (noted in black), during the electrodeposition process at the site shown in Figure 2a. (b) Distribution of NP displacement length $\triangle d_c$, monitored optically, for all the experiments and tip sizes. (c) Scheme depicting the possible aggregative (asymmetric vs symmetric) growth mechanism that induces the motion of the centroid of the optical features. (d) Polar distribution of angles reflecting the motion direction from the centre of the droplet for the same experiments depicted in (b). NP motion that involves a displacement of at least 30 nm is included in the polar plot.

Conclusion

In summary, we have demonstrated that coupled SECCM-IRM allows operando monitoring of nanoscale electrodeposition and the processes underlying the rapid formation of discrete NPs in a nanodroplet. With SECCM droplets ranging in area between 0.4 to 1 μm^2, one to six distinct NPs were detected per droplet, with a detection size limit estimated to ca. 60 nm in diameter. The hybrid method further reveals the dynamics of NP growth, with NPs progressively appearing on the WE surface within the first 3–15 ms of the electrodeposition. On a longer timescale (~ few 100 ms), the displacement of their centroid by 30–200 nm is seen. Coupled with the electrochemical signature, these observations suggest that the NPs are grown from the surface diffusion and aggregation of rapidly electrogenerated Ag nuclei (undetected optically), in agreement with recent nucleation-aggregation growth models. Beyond the unique mechanistic insights into electrodeposition, coupling a nanoscale electrochemical cell and optical monitoring paves the way for spatiotemporal analysis of single entity electrochemical dynamics with subdroplet resolution, ms temporal imaging resolution (beyond the current in situ imaging capabilities such as TEM). The approach could be generalised to other transparent electrodes, as high-resolution optical imaging has been demonstrated on nanoscale thin films of Au or graphene covering glass slides.[43–47] It will facilitate high throughput studies[48] of electrodeposition and nanoscale surface functionalization.

Experimental Section

Reagents and materials

Silver nitrate (AgNO$_3$, Sigma) and potassium nitrate (KNO$_3$, Sigma) were used as supplied by the manufacturer. Solutions were prepared with ultrapure deionised water (PURELAB Chorus, ELGA, UK).

Indium tin oxide (ITO) coated coverslips [20×20 mm×130 to 170 μm (thickness#1), with 70 nm nominal ITO coating thickness, SPI Supplies, USA] served as both the SECCM working electrode (WE) and as the IRM substrate. Before use, they were cleaned by sonication in isopropyl alcohol and subsequently in deionised water. Electrical connection to the substrate was provided by a tinned insulated copper wire (ca. 1 mm diameter), attached to the ITO coating with silver conductive paint (RS Components, UK), and secured with epoxy adhesive (Araldite, UK). ITO coverslips were glued to the bottom of the bottom of 3D-printed discs (polylactic acid material) with a ca.15mm diameter aperture: a picture of the elements of the opto-electrochemical cell is given in Figure S1.1, SI, section S1. A chloridized 0.125 mm diameter annealed silver wire (99.99%, Goodfellow, UK) was used as a quasi-reference counter electrode (QRCE). Applied voltage values reported herein are versus this QRCE.

SECCM-IRM workstation

The hybrid SECCM-IRM workstation, with pictures of the setup, is detailed in the Supporting Information, SI, section S1. Briefly, it was made in house using an inverted microscope (DMI4000B, Leica, Germany) and custom-built electronics (see SI, section S1). The ITO substrate surface was observed by a 63× oil immersion microscope objective (HCX Plan Apochromatic, NA=1.4, Leica) and back illuminated with the blue channel (intensity peak at 470 nm, bandwidth FWHM of 19 nm) of a multi-LED light source (Niji, Bluebox Optics, UK). Optical images were recorded with a CMOS digital camera (C11440-42U30, Hamamatsu Photonics, Japan) at rates of 327.5 frames per second.

The SECCM setup is composed of micro-positioning stages (details in SI, section S1) controlled by Labview 2019 (National instruments) user interface, running the Warwick Electrochemical scanning Probe Microscopy (WEC-SPM, www.warwick.ac.uk/electrochemistry) software enabling pipette and substrate motion as well as electrode potential control and current acquisition (through an FPGA card, USB-7856-R OEM, National instruments, U.S.A.).

The camera output trigger signal, a 3.3 V pulse per frame, was also recorded through the FPGA card, concurrently with the electrochemical measurements; thus allowing synchronous analysis and presentation of SECCM and IRM data. The optical microscope and positioning stages were mounted atop an active vibration isolation table (CleanBench, TMC, U.S.A.), and encased within a Faraday cage, lined with thermal isolation panels.

Pipette approach and meniscus landing experiments were monitored optically as detailed in SI, section S1. Each sequence (movies) of the landing experiments were cropped and analysed with a custom Python functions built using four distinct Python libraries: numpy, trackpy, pims and scipy. Details are given in section S4 and functions are provided in section S9.

ChemElectroChem

Research Article
doi.org/10.1002/celc.202201162

Chemistry Europe
European Chemical
Societies Publishing

Conflict of Interest

The authors declare no conflict of interest.

Data Availability Statement

The data that support the findings of this study are available from the corresponding author upon reasonable request.

Keywords: electrodeposition · nanopipette · optical microscopy · SECCM · single nanoparticle

[1] M. Grzelczak, J. Vermant, E. M. Furst, L. M. Liz-Marzán, *ACS Nano* **2010**, *4*, 3591–3605.
[2] J. Li, F. L. Deepak, *Chem. Rev.* **2022**, *122*, 16911–16982.
[3] T. Kraus, L. Malaquin, H. Schmid, W. Riess, N. D. Spencer, H. Wolf, *Nat. Nanotechnol.* **2007**, *2*, 570–576.
[4] L. Jiang, X. Chen, N. Lu, L. Chi, *Acc. Chem. Res.* **2014**, *47*, 3009–3017.
[5] H. Zhang, C. Kinnear, P. Mulvaney, *Adv. Mater.* **2020**, *32*, 1904551.
[6] D. V. Yakimchuk, U. V. Prigodich, S. E. Demyanov, J. Ustarroz, H. Terryn, K. Baert, S. A. Khubezhov, D. I. Tishkevich, A. V. Trukhanov, V. Sivakov, E. Y. Kaniukov, *Mater. Chem. Phys.* **2022**, *283*, 126016.
[7] R. Garcia, R. V. Martinez, J. Martinez, *Chem. Soc. Rev.* **2006**, *35*, 29–38.
[8] R.-J. Yu, Y.-L. Ying, R. Gao, Y.-T. Long, *Angew. Chem. Int. Ed.* **2019**, *58*, 3706–3714; *Angew. Chem.* **2019**, *131*, 3744–3752.
[9] K. McKelvey, S. R. German, Y. Zhang, H. S. White, M. A. Edwards, *Curr. Opin. Electrochem.* **2017**, *6*, 4–9.
[10] N. Ebejer, A. G. Güell, S. C. S. Lai, K. McKelvey, M. E. Snowden, P. R. Unwin, *Annu. Rev. Anal. Chem.* **2013**, *6*, 329–351.
[11] Y. Wang, H. Cai, M. V. Mirkin, *ChemElectroChem* **2015**, *2*, 343–347.
[12] S. R. German, L. Luo, H. S. White, T. L. Mega, *J. Phys. Chem. C* **2013**, *117*, 703–711.
[13] S. E. F. Kleijn, S. C. S. Lai, T. S. Miller, A. I. Yanson, M. T. M. Koper, P. R. Unwin, *J. Am. Chem. Soc.* **2012**, *134*, 18558–18561.
[14] Y.-R. Kim, S. C. S. Lai, K. McKelvey, G. Zhang, D. Perry, T. S. Miller, P. R. Unwin, *J. Phys. Chem. C* **2015**, *119*, 17389–17397.
[15] S. C. S. Lai, R. A. Lazenby, P. M. Kirkman, P. R. Unwin, *Chem. Sci.* **2015**, *6*, 1126–1138.
[16] S. Daryadel, A. Behroozfar, S. R. Morsali, S. Moreno, M. Baniasadi, J. Bykova, R. A. Bernal, M. Minary-Jolandan, *Nano Lett.* **2018**, *18*, 208–214.
[17] S. Daryadel, A. Behroozfar, M. Minary-Jolandan, *Adv. Eng. Mater.* **2019**, *21*, 1800946.
[18] D. Momotenko, A. Page, M. Adobes-Vidal, P. R. Unwin, *ACS Nano* **2016**, *10*, 8871–8878.
[19] J. Hengsteler, B. Mandal, C. van Nisselroy, G. P. S. Lau, T. Schlotter, T. Zambelli, D. Momotenko, *Nano Lett.* **2021**, *21*, 9093–9101.
[20] M. M. Rahman, C. L. Tolbert, P. Saha, J. M. Halpern, C. M. Hill, *ACS Nano* **2022**, *16*, 21275–21282.
[21] J. Ustarroz, M. Kang, E. Bullions, P. R. Unwin, *Chem. Sci.* **2017**, *8*, 1841–1853.
[22] J. Ustarroz, *Curr. Opin. Electrochem.* **2020**, *19*, 144–152.
[23] J. Ustarroz, J. A. Hammons, T. Altantzis, A. Hubin, S. Bals, H. Terryn, *J. Am. Chem. Soc.* **2013**, *135*, 11550–11561.
[24] I. M. Ornelas, P. R. Unwin, C. L. Bentley, *Anal. Chem.* **2019**, *91*, 14854–14859.
[25] J.-F. Lemineur, H. Wang, W. Wang, F. Kanoufi, *Annu. Rev. Anal. Chem.* **2022**, *15*, 57–82.
[26] F. Kanoufi, *Encycl. Electrochem.*, Wiley **2021**, pp. 1–80, 10.1002/9783527610426.bard030108.
[27] D. Valavanis, P. Ciocci, G. N. Meloni, P. Morris, J.-F. Lemineur, I. J. McPherson, F. Kanoufi, P. R. Unwin, *Faraday Discuss.* **2022**, *233*, 122–148.
[28] L. Godeffroy, J.-F. Lemineur, V. Shkirskiy, M. Miranda Vieira, J.-M. Noël, F. Kanoufi, *Small Methods* **2022**, *6*, 2200659.
[29] J.-F. Lemineur, P. Ciocci, J.-M. Noël, H. Ge, C. Combellas, F. Kanoufi, *ACS Nano* **2021**, *15*, 2643–2653.
[30] L. Godeffroy, P. Ciocci, A. Nsabimana, M. Miranda Vieira, J.-M. Noël, C. Combellas, J.-F. Lemineur, F. Kanoufi, *Angew. Chem. Int. Ed.* **2021**, *60*, 16980–16983; *Angew. Chem.* **2021**, *133*, 17117–17120.
[31] R. Hao, Y. Fan, B. Zhang, *J. Am. Chem. Soc.* **2017**, *139*, 12274–12282.
[32] G. Sandmann, H. Dietz, W. Plieth, *J. Electroanal. Chem.* **2000**, *491*, 78–86.
[33] M. Ueda, H. Dietz, A. Anders, H. Kneppe, A. Meixner, W. Plieth, *Electrochim. Acta* **2002**, *48*, 377–386.
[34] P. Saha, J. W. Hill, J. D. Walmsley, C. M. Hill, *Anal. Chem.* **2018**, *90*, 12832–12839.
[35] V. Sundaresan, J. W. Monaghan, K. A. Willets, *J. Phys. Chem. C* **2018**, *122*, 3138–3145.
[36] J.-F. Lemineur, J.-M. Noël, A. Courty, D. Ausserré, C. Combellas, F. Kanoufi, *J. Am. Chem. Soc.* **2020**, *142*, 7937–7946.
[37] K. A. Willets, *ACS Nano* **2019**, *13*, 6145–6150.
[38] T. Liu, S. Liu, W. Jiang, W. Wang, *ACS Nano* **2019**, *13*, 6279–6286.
[39] W. Jiang, W. Wei, T. Yuan, S. Liu, B. Niu, H. Wang, W. Wang, *Chem. Sci.* **2021**, *12*, 8556–8562.
[40] E. J. Harbron, P. F. Barbara, *J. Chem. Educ.* **2002**, *79*, 211.
[41] H. E. M. Hussein, R. J. Maurer, H. Amari, J. J. P. Peters, L. Meng, R. Beanland, M. E. Newton, J. V. Macpherson, *ACS Nano* **2018**, *12*, 7388–7396.
[42] J. E. Evans, K. L. Jungjohann, N. D. Browning, I. Arslan, *Nano Lett.* **2011**, *11*, 2809–2813.
[43] J.-F. Lemineur, J.-M. Noël, D. Ausserré, C. Combellas, F. Kanoufi, *Angew. Chem. Int. Ed.* **2018**, *57*, 11998–12002; *Angew. Chem.* **2018**, *130*, 12174–12178.
[44] S. Campidelli, R. Abou Khachfe, K. Jaouen, J. Monteiller, C. Amra, M. Zerrad, R. Cornut, V. Derycke, D. Ausserré, *Sci. Adv.* **2017**, *3*, e1601724.
[45] W. Li, M. Wojcik, K. Xu, *Nano Lett.* **2019**, *19*, 983–989.
[46] L. Godeffroy, P. Ciocci, J.-F. Lemineur, F. Kanoufi, *Curr. Opin. Electrochem.* **2022**, *36*, 101165.
[47] J.-F. Lemineur, J.-M. Noël, C. Combellas, D. Ausserré, F. Kanoufi, *Faraday Discuss.* **2018**, *210*, 381–395.
[48] X. Xu, D. Valavanis, P. Ciocci, S. Confederat, F. Marcuccio, J.-F. Lemineur, P. Actis, F. Kanoufi, P. R. Unwin, *Anal. Chem.* **2022**, *95*, 319–356.

RESEARCH ARTICLE

Electrodeposition of limited number of nanoparticles requires confinement within nano-electrochemical cells. Super-localization optical microscopy reveals operando the process dynamics: within the first 3–13 ms the delayed formation of one to six distinct nanoparticles is detected per droplet; later the displacement of their centroid suggests the importance of aggregation and surface diffusion.
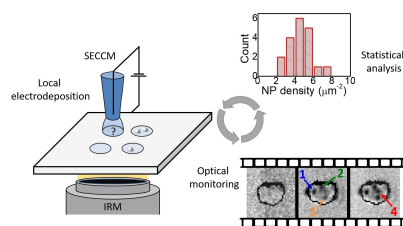
P. Ciocci, D. Valavanis, Dr. G. N. Meloni, Dr. J.-F. Lemineur, Dr. P. R. Unwin*, Dr. F. Kanoufi*

1 – 7

Optical Super-Localisation of Single Nanoparticle Nucleation and Growth in Nanodroplets